Planet-Sun Sensor Revisited

Dario Modenini,[1] and Marco Zannoni.[2]
University of Bologna, I-47121, Italy

Since the seminal work of Daniele Mortari published in this journal in 1997, the concept of an attitude sensor using images of illuminated celestial bodies has been pushed forward through the years. The basic idea consists of extracting two independent directions from the image of a celestial body, namely the camera-to-planet and the planet-to-Sun directions. The former is estimated from the center of an ellipse fitted to the imaged limb points, the latter from the symmetry axis of the illuminated region. These assumptions, however, only hold for far-distant spherical targets. In this work, we reformulate the problem in the framework of projective camera transformations of quadrics and conics, and present an algorithm estimating the line-of-sight to the planet and the illumination direction from the limb and terminator ellipses, respectively. The method is applicable to any ellipsoid-like celestial body having known orientation. The algorithm is first validated on synthetically generated images and then tested using real pictures of Dione and Enceladus satellites gathered from Cassini spacecraft. Results show that our sensor concept returns root mean squared errors in the order of the angular width of a pixel in computing the nadir direction, and sub-degree accuracy in computing the Sun direction.

Nomenclature

a,b,c =   ellipsoid radii, m

C =   3x3 homogeneous conic matrix

D =   diagonal matrix

e =   ellipticity

f =   focal length, m

---

k	=	dimensionless range
K	=	matrix of intrinsic camera parameters
M	=	terminator ellipse semi-major axis
m	=	terminator ellipse semi-minor axis
$\mathbf{n}$	=	terminator plane normal unit vector
Q	=	4x4 quadric matrix
Q_3	=	3x3 quadric matrix
R	=	attitude matrix
S	=	signature matrix
$\mathbf{s}$	=	Sun position vector, m
T	=	3x3 homogeneous terminator matrix
$\mathbf{t}$	=	translation vector, m
V,W	=	eigenvector matrices
α	=	nadir direction error angle
β	=	Sun direction error angle
$\mathcal{E}$	=	Euclidean transformation matrix
λ	=	latitude
$\mathbf{v}$	=	line-of-sight unit vector
ρ	=	range, m
τ	=	longitude

Subscripts

c	=	camera frame
n	=	North-East-Down frame
t	=	terminator frame
w	=	world frame

Superscripts

*	=	adjugate or inverse
T	=	transpose

I. Introduction

THE determination of spacecraft attitude from a set of vector observations is a recurrent problem, that has been extensively studied for many decades. Indeed, most attitude sensors consists of determining the body axes components of a unit direction vector or line-of-sight (LOS). Common examples are Sun sensors, magnetometers and nadir sensors. Since a LOS measurement encodes two scalar information, at least two independent LOS observations are required to reconstruct the triaxial attitude of a spacecraft. Most often, one attitude sensor provides a single LOS, so that at least two sensors are needed. A well-known remarkable exception is represented by star trackers, which are cameras capable of tracking multiple stars' LOS vectors.

Camera based attitude sensors can also be employed to track a larger target in the FOV, such as a planet or a moon. Then, if the target is only partially illuminated, both the LOS from the camera to the body and the LOS from the body to the Sun (i.e. the illumination direction) can be retrieved from the image. Once these are known, the attitude can be reconstructed using any classic method available for solving the attitude determination problem from vector observations, i.e. the so called Wahba's problem [1]. This idea, which we may refer to as the planet-Sun sensor, was originally proposed by Mortari in [2], and later refined by Park and Mortari in [3]. More recently, the same concept was pushed forward by Enright, as a moon-tracking backup mode for star trackers [4], and applied on board of μ-LabSat spacecraft for triaxial attitude estimation from Earth images [5].

In the planet-Sun attitude sensor concept, the attitude solution is provided in two steps. First, the local nadir direction is computed from the center of the imaged limb ellipse. Second, it is assumed that the limb and terminator curves share a common axis, i.e. a principal and symmetry axis of the illuminated area (see Fig.1a), which is used to estimate the direction of illumination.

In both steps, there are some implicit assumptions which must hold, namely, that the target is a sphere and that its size is much smaller than the range from the camera. The latter is needed since the center of an imaged ellipsoid is mapped onto the center of the imaged ellipse through a camera projective transformation only if the target is at infinite distance; the sphericity is instead required since for a generic triaxial ellipsoid the illuminated region has no symmetry axis, nor the direction of illumination is coincident with a principal axis (see Fig. 1). Nevertheless, the above assumptions are often justified in practical applications since celestial bodies have very low flattening and the target is indeed very far, yet they may introduce errors in the estimate.

Recently, the attitude determination problem has been tackled in the framework of ellipsoid observations, rather than from LOS measurements as per the classical Wahba problem. In [6] it was shown that from a single observation of an ellipsoidal celestial body, a closed form formulation for the attitude matrix can be obtained by solving a quadric-to-conic correspondence problem. The theoretical framework was later applied to infrared images of an ellipsoid, to develop a triaxial horizon sensor [7]. Unfortunately, celestial bodies feature typically a very small degree of polar or equatorial (if any) oblateness, so that, in practice, the orientation about camera boresight can be only loosely constrained using such a sensor as a standalone source for the attitude.

In this paper, we revisit the planet-Sun attitude sensor in light of the theory of attitude determination from ellipsoid observations, to provide an algorithm which is generally applicable to any ellipsoid-like celestial body without further restrictive assumptions. The revisited planet-Sun sensor relies on the theory of perspective transformations of quadrics (i.e. the planet) and conics (i.e. the terminator curve on planet's surface) under the action of a pin-hole camera, both of which are well known [8]. In particular, it formulates and solves the attitude determination problem through joint quadric-conic and conic-conic correspondences. Despite the quadric-conic correspondence problem alone has been already successfully tackled for computing whether the attitude [6, 7], position [9-13] or a combination of both [14, 15] from ellipsoids limb, to the best of the authors' knowledge a general framework for estimating the direction of the light partially illuminating an ellipsoid has not been tackled yet, neither alone, nor together with the LOS to develop a full attitude sensor.

The resulting sensor concept can be applied for real-time applications onboard a spacecraft, which aims at estimating its attitude relative to a planetary target being imaged in partial illumination conditions, and without resorting to inertial attitude knowledge from star-tracking, provided that the inertial orientation of the planet is known.

The manuscript is organized as follows. In Section II, we first recall the mathematical background of pinhole projective transformation and its action onto quadric surfaces. Sub-section II.A faces the problem of computing the line-of-sight vector from the limb ellipse. Two alternative solutions are discussed for this problem: one, derived from previously published results [6, 7], allows computing the LOS as a byproduct of the entire attitude matrix estimate; the other, instead, directly computes the line-of-sight only. Sub-section II.B deals with the computation of the illumination direction. First, the terminator ellipse is computed as the intersection of a plane and the target ellipsoid; then, by the study of the planar homography mapping the terminator conic onto the image plane, an estimate of the normal to the terminator plane is sought for, from which the illumination direction can be retrieved. Section III presents

the algorithm validation against synthetically generated images. In Section IV, the algorithm performance is assessed under a representative scenario, making use of Dione and Enceladus images gathered by Cassini spacecraft. Finally, a discussion on the main outcomes of this study is found in Section V.

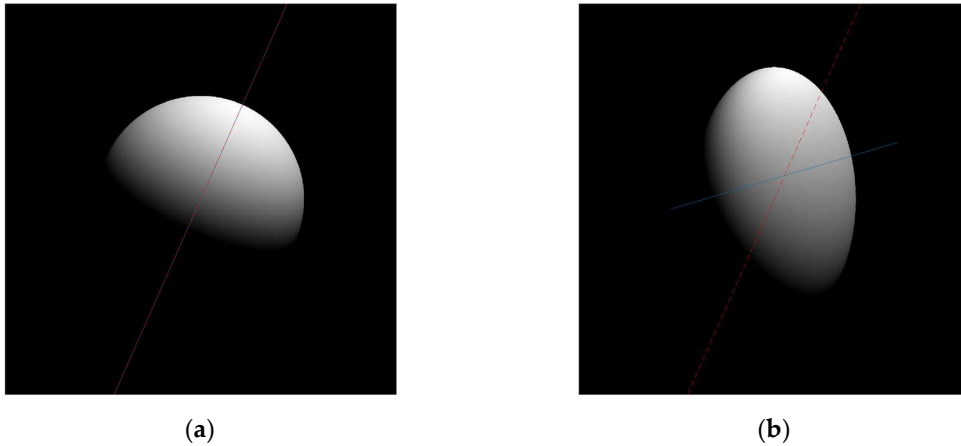(a)   (b)

Fig. 1 Synthetic images of illuminated quadric surfaces with direction of illumination (dotted red line) and principal axis of illuminated area (solid blue line). (a) sphere (the two directions coincide); (b) triaxial ellipsoid.

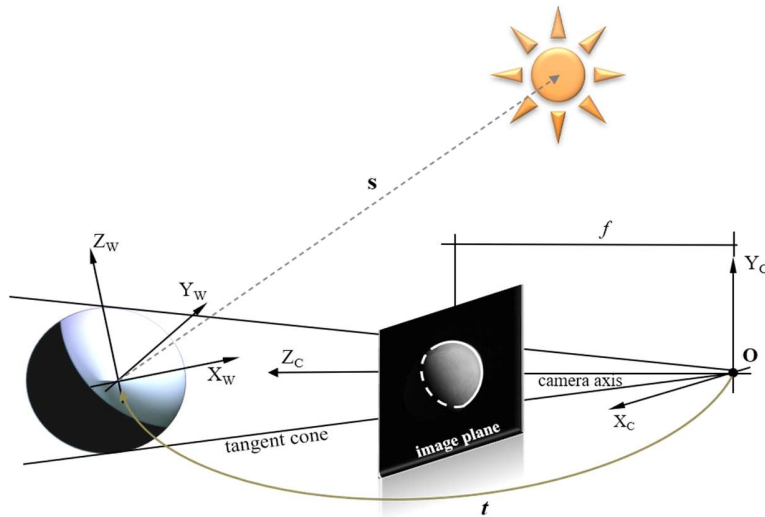## II. Theory of attitude determination from illuminated ellipsoids

Fig. 2 Graphical representation of the imaging of an illuminated celestial body with a pinhole camera.

We will approach the problem of computing the attitude of a spacecraft from an image of an illuminated ellipsoid using the framework of projective camera transformations [8], assuming the relative position to be known. The

scenario is depicted in Figure 2, where a partially illuminated ellipsoid and the image plane are represented. The imaged contour of the ellipsoid is the intersection of the cone tangent to the ellipsoid itself and whose vertex is lying on the camera center with the image plane; this intersection is the limb conic, whose visible portion is highlighted with a full white line in the figure. On the other hand, the terminator ellipse, denoted with a dashed line in the figure, is the image of the conic resulting from the intersection of a plane having normal **n**, whose orientation depends on the illumination direction[3]. The mapping of a quadric surface and a plane ellipse under a projective camera transformation are both known and will be briefly recalled in the following.

Under the Euclidean transformation $\mathcal{E} = R[I \quad t_w]$, the quadric Q transforms to the conic C on the image plane of a pinhole camera, according to [8]:

$$K^{-1}C^*K^{-T} \propto \mathcal{E}Q^*\mathcal{E}^T. \tag{1}$$

In Eq. (1), Q is the matrix:

$$Q = \begin{bmatrix} 1/a^2 & 0 & 0 & 0 \\ 0 & 1/b^2 & 0 & 0 \\ 0 & 0 & 1/c^2 & 0 \\ 0 & 0 & 0 & -1 \end{bmatrix} = \begin{bmatrix} Q_3 & \mathbf{0} \\ \mathbf{0}^T & -1 \end{bmatrix}, \tag{2}$$

a, b, c, being the ellipsoid semi-axes lengths; R is the orthogonal attitude matrix mapping from the world frame, defined by the ellipsoid axes, to the camera frame (the unknown to be estimated); t_w is the translation vector from the camera center to the origin of the target ellipsoid expressed in world frame (assumed known); C^* is the adjugate[4] of the conic matrix C computed from the coefficients of the ellipse quadratic equation:

$$Ax^2 + Bxy + Dy^2 + Ex + Fy + G = 0 \leftrightarrow [x \; y \; 1]C\begin{bmatrix} x \\ y \\ 1 \end{bmatrix} = 0,$$

$$C = \begin{bmatrix} A & \dfrac{B}{2} & \dfrac{E}{2} \\ \dfrac{B}{2} & D & \dfrac{F}{2} \\ \dfrac{E}{2} & \dfrac{F}{2} & G \end{bmatrix}, \qquad C^* = \begin{bmatrix} F^2 - 4DG & 2BG - EF & 2DE - BF \\ 2BG - EF & E^2 - 4AG & 2AF - BE \\ 2DE - BF & 2AF - BE & B^2 - 4AD \end{bmatrix}, \tag{3}$$

and K is the intrinsic camera matrix, representing the projective transformation. For a pinhole camera with optical axis coincident with body axis z and the pixel array plane coincident with body x-y plane, $K = \begin{bmatrix} f_x & s & p_x \\ 0 & f_y & p_y \\ 0 & 0 & 1 \end{bmatrix}$, where f_x, f_y

---

[3] For the special case of a spherical body, **n** is coincident with the illumination direction.

is the focal vector and p_x, p_y are the coordinates of the principal point, and s is the skew-angle (equal zero for orthogonal x-y axes). The coordinates of the ellipse center can be computed directly from the elements of C^* as in:

$$x_o = C^*(1,3)/C^*(3,3) \quad y_o = C^*(2,3)/C^*(3,3). \tag{4}$$

Note that, since Q (C) matrix represents an ellipsoid (ellipse) in homogeneous coordinates, it is invariant to a common scaling of all its elements. Scaling invariance thus holds for Eq. (1) as well, which maps between the adjugate/inverse quadric matrix, and the adjugate/inverse imaged conic matrix. Moreover, since an ellipsoid (ellipse) is a non-degenerate quadric (conic), one can indifferently assign to * the meaning of adjugate or inverse. From a geometric point of view, Q^* (C^*) describes the so-called dual, or envelope, quadric (conic) which defines the planes (lines) tangent to Q (C). An equivalent relation between the point quadric Q and the point conic C may also be derived, by considering the back-projection of the imaged ellipse as the ellipsoid tangent cone, or by direct inversion of Eq. (1), see e.g. [10,11,15].

By defining matrices:

$$C = K^T C K, \qquad B = Q_3^* - \rho^2 \boldsymbol{v}_w \boldsymbol{v}_w^T, \tag{5}$$

ρ being the range to the target and $\boldsymbol{v}_w$ the unit vector expressed in the target (or world) frame. Eq. (1) can then be rewritten as:

$$C^* \sim R(Q_3^* - \rho^2 \boldsymbol{v}_w \boldsymbol{v}_w^T)R^T = RBR^T. \tag{6}$$

Equation (6) is a special case of the hand-eye calibration problem [17], which can be solved after computing the spectral decompositions of C^* and B.

Such an approach was followed in [6,7] for computing the whole attitude matrix from a single ellipsoid observation. Nevertheless, those works highlighted that imaging a target with low flattening, as most of the celestial bodies, the detectability of the rotation around the boresight is severely degraded. Here, instead, we assume to detect a terminator ellipse besides the limb one which allows us to pursue an alternative approach, by combining the information of the LOS direction in camera frame, $\boldsymbol{v}_c$, extracted from the planetary limb, to the direction of illumination estimated from the terminator. This is, indeed, the main concept of a planet-Sun sensor.

A. Computation of the LOS direction from the limb ellipse

Computing the LOS is the fundamental step also in the original formulation of the planet-Sun attitude sensor [2,3] and in similar works [4,5]. In most references it is assumed that the LOS vector from the camera center to the target passes through the center of the image outline (whether this last is assumed to be a circle or an ellipse). However, for

a planet at finite distance, the LOS $\boldsymbol{v}_c$ is *not* mapped onto the center of the imaged conic, as it must follow the transformation prescribed by Eq. (1).

In the following we will study how the LOS is related to the conic center, first considering the special case of a spherical target. To this end, it is convenient to rearrange Eq.(6) as:

$$C^* \sim R\breve{Q}_3^* R^T - \boldsymbol{v}_c \boldsymbol{v}_c^T, \tag{7}$$

where the quadric matrix Q_3^* is rendered dimensionless by defining $\breve{Q}_3^* = Q_3^*/\rho^2$. For a sphere, $\breve{Q}_3^* = a^2/\rho^2 I = k^2 I$, so that $R\breve{Q}_3^* R^T = \breve{Q}_3^*$. For ease of notation, we further assume an ideal pinhole-camera matrix having principal point coincident to the origin and no skew, for which $K=\text{diag}([f\,f\,1])$. Then, it is easy to verify that under these hypotheses the adjugate conic matrix reads:

$$C^* \sim K\left(\breve{Q}_3^* - \boldsymbol{v}_c \boldsymbol{v}_c^T\right)K^T = \begin{bmatrix} f^2(k^2 - v_1^2) & -f^2 v_1 v_2 & -f v_1 v_3 \\ -f^2 v_1 v_2 & f^2(k^2 - v_2^2) & -f v_2 v_3 \\ -f v_1 v_3 & -f v_2 v_3 & (k^2 - v_3^2) \end{bmatrix}. \tag{8}$$

According to Eq. (4), the center of the conic is:

$$x_o = f\frac{v_1 v_3}{v_3^2 - k^2}, \quad y_o = f\frac{v_2 v_3}{v_3^2 - k^2}, \tag{9}$$

or, dividing by the focal length:

$$\frac{x_o}{f} = \frac{C_{(1,3)}^*}{C_{(3,3)}^*} = \frac{v_1}{v_3} \cdot \frac{1}{1 - (k/v_3)^2}, \quad \frac{y_o}{f} = \frac{C_{(2,3)}^*}{C_{(3,3)}^*} = \frac{v_2}{v_3} \cdot \frac{1}{1 - (k/v_3)^2}. \tag{10}$$

Clearly, the conic center depends on both the LOS vector and the range to the spherical target, and it lies on the LOS only for

$$\frac{1}{1 - (k/v_3)^2} = 1, \tag{11}$$

which is approximately true in the limit $k/v_3 \to 0$, i.e. when the sphere is at an infinite distance. Note that the limit of k/v_3 is always defined, provided that $v_3 \neq 0$, which is in turn true if the camera points towards the target. Furthermore, for an ideal pinhole camera, k can be related to the camera field of view (FoV) as:

$$k = \frac{a}{\rho} \cong \frac{s}{f} \cong w_\% \tan\left(\frac{\text{FoV}}{2}\right), \tag{12}$$

where s is the size (radius) of the body on the image plane and $w_\%$ is the percentage width of the imaged conic with respect to the image size.

Eq. (12) indicates that the LOS offset from the ellipse center due to the finite distance of the target falls of rapidly for instruments having a narrow FoV, as commonly happens for navigation cameras. Remarkably, this is not always the case for cameras employed as Earth sensors, for which the FOV may be on the order of 1 rad. In such a case, the left-hand side in (12) may differ from unity of some tens of percent. Furthermore, wide-angle cameras are becoming relevant also in deep space missions, see e.g. the JunoCam [18] and JPL's Advanced Pointing Imaging Camera (APIC) concept [19].

If we express the LOS as a function of the boresight angle, θ, and the azimuth φ from the x detector axis, these can be computed from the conic coefficients as:

$$\varphi = \text{atan}\left(-C^*_{(2,3)}, -C^*_{(1,3)}\right) \quad \theta = \text{acos}\left(k^2 - C^*_{(3,3)}\right) \tag{13}$$

Note that, for a spherical target, the value of range ρ needed to compute k needs not to be known in advance by independent means, since it can be computed directly from the eigenvalues of C^*, as shown in [14].

For a generic triaxial ellipsoids the above analysis would complicate significantly. By considering a spheroid (i.e. an ellipsoid of revolution), the counterpart of Eq. (10) is a bit cumbersome, but still manageable (see Appendix), and it indicates that the ellipse center departs from the LOS direction by an extent which depends in general on the range, the flattening and, most important, on the camera orientation itself. Therefore, it is difficult to state any bound on the error performed by estimating the LOS direction from the conic center only.

These considerations motivate the quest for a LOS solution which is fully consistent with the projective camera transformation (1). To this end, one can pursue two paths.

First, we note that Eq.(7) states that there exists a rank-one, unit norm perturbation to C^* matrix which renders it orthogonally similar to $\breve{Q}^*_3$, apart from scaling. The scaling ambiguity can be easily removed by taking the trace of both side of Eq.(7) and multiplying C^* by $[\text{tr}(\breve{Q}^*_3) - 1]/\text{tr}(C^*)$.

One thus need to write two equations for the two independent $\boldsymbol{v}_c$ components exploiting some matrix invariants to orthogonal transformations. For example, two such equations are:

$$\begin{aligned}
\det(C^* + \boldsymbol{v}_c\boldsymbol{v}_c^T) &= \det(\breve{Q}^*_3) \\
\text{tr}[(C^* + \boldsymbol{v}_c\boldsymbol{v}_c^T)^2] &= \text{tr}\left(\breve{Q}^{*2}_3\right)
\end{aligned} \tag{14}$$

Equations (14) can be rearranged into explicit functions of $\boldsymbol{v}_c$ exploiting the matrix determinant lemma and the cyclic trace property, to yield:

$$\boldsymbol{v}_c^T \mathcal{C} \boldsymbol{v}_c = \frac{\det(\breve{Q}_3^*)}{\det(\mathcal{C}^*)} - 1$$
$$2\boldsymbol{v}_c^T \mathcal{C}^* \boldsymbol{v}_c = \mathrm{tr}\left(\breve{Q}_3^{*2}\right) - \mathrm{tr}(\mathcal{C}^{*2}) - 1 \tag{15}$$
$$\text{subject to: } \boldsymbol{v}_c^T \boldsymbol{v}_c = 1$$

This system of constrained second order polynomial equations can be solved for $\boldsymbol{v}_c$, provided that the range ρ is known, by using an iterative root-finding method such as Newton-Raphson. A suitable initial condition is the one obtained from the imaged ellipse center:

$$\boldsymbol{v}_{0,c} = \frac{1}{\mathcal{C}_{(3,3)}^*}\left[\mathcal{C}_{(1,3)}^* \quad \mathcal{C}_{(2,3)}^* \quad \sqrt{\mathcal{C}_{(3,3)}^{*2} - \mathcal{C}_{(1,3)}^{*2} - \mathcal{C}_{(2,3)}^{*2}}\right]. \tag{16}$$

In Eq. (16) the sign of the third component of $\boldsymbol{v}_{0,c}$ is set positive, to ensure that the camera is pointing towards (and not away from) the target. Solution to Eq. (15), being evaluated iteratively is not very attractive for onboard implementations. Furthermore, our numerical tests revealed that the number of iterations may get high before convergence is reached.

An alternative method to estimate $\boldsymbol{v}_c$ involves reformulating Eq. (6) with respect to a Local-Vertical-Local-Horizon (LVLH) frame, so that the LOS direction is coincident with one of the columns of the attitude matrix R, similar to as done in [14]. For example, by adopting a north–east–down (NED) frame, matrix R can be written as the combination of two rotations:

$$R = R_{c/n}R_{n/w}, \tag{17}$$

where $R_{n/w}$ is the rotation matrix from the world to NED frame, function of the vantage direction $\boldsymbol{v}_w$, while $R_{c/n}$ is the rotation matrix from NED to camera frame, whose third column is indeed $\boldsymbol{v}_c$. Then, following the method in [7], one can show that Eq.(6) can be rearranged having as unknown matrix $R_{c/n}$ as:

$$\mathcal{C}^* \sim R_{c/n}\tilde{B}_n R_{c/n}^T, \tag{18}$$

with

$$\tilde{B}_n = R_{n/w}\tilde{Q}_3^* R_{n/w}^T - \tilde{\rho}^2 [0 \quad 0 \quad 1]^T[0 \quad 0 \quad 1], \tag{19}$$

$\tilde{Q}_3^* = \frac{Q_3^*}{a^2} = \mathrm{diag}\left(\left[1, \frac{b^2}{a^2}, \frac{c^2}{a^2}\right]\right)$ and $\tilde{\rho} = \rho/a^2$ is a dimensionless range which can be computed provided $\boldsymbol{v}_w$ is known, see [7] for details.

Once $\tilde{B}_n^*$ is available, it is easy to verify that a solution to Eq. (18) can be computed as:

$$R_{c/n} = VSW^T, \tag{20}$$

where V and W the eigenvector matrices respectively of C^* and $\tilde{B}_n$, and S is the 3×3 signature matrix. Or, since we are interested only in $\boldsymbol{v}_c$:

$$\boldsymbol{v}_c = VS\mathbf{w}_3^T \qquad (21)$$

where $\mathbf{w}_3$ denotes the 3rd row of W. Note that Eqs. (20) and (21) leave the sign undetermined. However, of the eight possible signs combinations of matrix S, four only lead to a proper rotation matrix having determinant equal to +1. Of these four, only the two leading to a positive third component of $\boldsymbol{v}_c$ are admissible. As shown in [6], the residual ambiguity corresponds to two undistinguishable attitude configurations having opposite orientations of both x and y camera axes, due to the two symmetry planes of an ellipsoid. The correct quadrant in the image plane shall be chosen in agreement with the position of the ellipse center in the image.

As a final remark, it is worth noting that the two alternative solutions presented herein for the LOS, Eq. (15) and Eq.(21), require different pieces of information concerning the relative position between the camera and the target: the former requires the range, the latter $\boldsymbol{v}_w$ (i.e. the latitude/longitude of observation).

B. Computation of Sun direction from terminator ellipse

The terminator curve, which separates the lit and unlit part of the ellipsoid, can be defined as the contour generator of a central projection centered at the Sun. As such, it is the set of points on Q at which the light rays are tangent to the surface. Since a quadric defines a polarity between a point and a plane [1], the contour generator for a quadric surface under a central projection is the polar plane of the Sun position vector $\mathbf{s}$ with respect to Q, thus having equation:

$$[\mathbf{s} \quad 1]^T Q[\mathbf{x} \quad 1] = 0, \qquad (22)$$

where $\mathbf{x}=[x\ y\ z]^T$, $\mathbf{s}=[s_x\ s_y\ s_z]^T$, and all vectors are intended in world frame, unless otherwise stated. The normal of the terminator plane follows as:

$$\mathbf{n} = \begin{bmatrix} s_x/a^2 \\ s_y/b^2 \\ s_z/c^2 \end{bmatrix}; \qquad (23)$$

the terminator generator is the intersection of such a plane with the quadric surface, hence an ellipse.

There are different algorithms in the open literature for computing the intersection of a plane with a quadric. Here we will briefly recall the solution from [16]. We denote with T the terminator ellipse matrix and with $\mathcal{T}$ the image of such a conic. We consider a terminator reference frame defined by the triad $\mathbf{u}$-$\mathbf{v}$-$\mathbf{n}$, where $\mathbf{n}$ is the unit normal to the terminator plane, and $\mathbf{u}$, $\mathbf{v}$ are the major and minor ellipse axes directions (see Figure 3). With such a choice:

$$T = \text{diag}\left\{\frac{1}{M^2}, \frac{1}{m^2}, -1\right\}, \tag{24}$$

with M, m denoting the semi-major and semi-minor axes lengths.

Following [16], the semi-axes lengths and directions can be computed starting from any triad $\tilde{\mathbf{u}}$-$\tilde{\mathbf{v}}$-$\mathbf{n}$, $\tilde{\mathbf{u}}$-$\tilde{\mathbf{v}}$ being trial orthogonal unit vectors, by prescribing the relations:

$$\mathbf{u}^T Q_3 \mathbf{v} = \mathbf{v}^T Q_3 \mathbf{u} = 0. \tag{25}$$

In particular, $\mathbf{u}$ and $\mathbf{v}$ can be computed through the planar rotation:

$$\mathbf{u} = \cos\omega\tilde{\mathbf{u}} + \sin\omega\tilde{\mathbf{v}}\,; \quad \mathbf{v} = -\sin\omega\tilde{\mathbf{u}} + \cos\omega\tilde{\mathbf{v}}, \tag{26}$$

where $\omega = \frac{1}{2}\arctan\left(\frac{2\tilde{\mathbf{u}}^T Q_3 \tilde{\mathbf{v}}}{\tilde{\mathbf{u}}^T Q_3 \tilde{\mathbf{u}} - \tilde{\mathbf{v}}^T Q_3 \tilde{\mathbf{v}}}\right)$. The semi-axes lengths then are computed as:

$$M^2 = \frac{1}{\mathbf{u}^T Q_3 \mathbf{u}}, m^2 = \frac{1}{\mathbf{v}^T Q_3 \mathbf{v}}. \tag{27}$$

and T matrix is fully determined in the terminator frame. The transformation matrix from terminator to world frame directly follows as:

$$R_{w,t} = [\mathbf{u} \quad \mathbf{v} \quad \mathbf{n}]. \tag{28}$$

When captured by a projective camera, a conic T is mapped to the image plane onto another ellipse T' through a planar homography H, according to [8]:

$$T' \sim H^{-T} T H^{-1}, \tag{29}$$

where $H = K[\mathbf{r}_1 \quad \mathbf{r}_2 \quad \rho\mathbf{v}_c]$, $\mathbf{r}_i$ being columns of $R_{c,t}$.
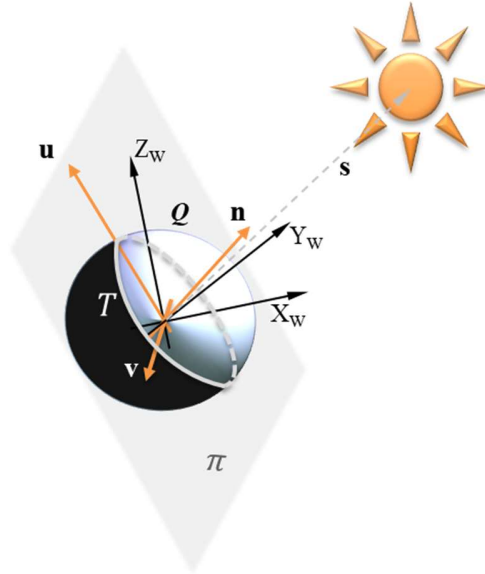

Fig. 3 Terminator line resulting from the intersection of a plane with normal n and the planet's surface.

Defining matrix $\mathcal{T} = K^T T' K$, Eq. (29) can be rearranged as:

$$\mathcal{T}^* \sim R_{c,t} T^* R_{c,t}^T - \rho^2 \boldsymbol{v}_c \boldsymbol{v}_c^T = R_{c,t}(T^* - \rho^2 \boldsymbol{v}_t \boldsymbol{v}_t^T)R_{c,t}^T, \tag{30}$$

where $R_{c,t}$ represents the rotation matrix from the terminator to the camera reference frame, $\boldsymbol{v}_t = R_{w,t}^T \boldsymbol{v}_w$ and

$$T^* = \text{diag}\{M^2, m^2, 0\}. \tag{31}$$

Eq. (30) is formally identical to Eq. (7), with the main difference that here T^* is not invertible as Q^*. Two options are now available for estimating the direction of illumination in camera frame from the terminator ellipse. Both rely on finding the components on the terminator plane normal in camera frame, $\mathbf{n}_c$, and then invert Eq. (23), while differing in the way $\mathbf{n}_c$ is estimated. First, we can search for a direct estimate of $\mathbf{n}_c$ exploiting $\boldsymbol{v}_c$ as estimated from the previous limb processing step. Indeed, Eqs. (30) and (31) indicate that matrix $\mathcal{T}^* + \rho^2 \boldsymbol{v}_c \boldsymbol{v}_c^T$ must have rank 2. Therefore, $\mathbf{n}_c$ is its null space:

$$\mathbf{n}_c = \text{null}(\mathcal{T}^* + \rho^2 \boldsymbol{v}_c \boldsymbol{v}_c^T). \tag{32}$$

In practice, being the terminator ellipse fitted from noisy data and $\boldsymbol{v}_c$ affected by error, $\mathcal{T}^* + \rho^2 \boldsymbol{v}_c \boldsymbol{v}_c^T$ will not be rank deficient. We can hence estimate $\mathbf{n}_c$ from the eigenvector associated with the smallest singular value of $\mathcal{T}^* + \rho^2 \boldsymbol{v}_c \boldsymbol{v}_c^T$, i.e. from its rank-2 matrix approximation.

Alternatively, one can solve for the entire terminator-to-camera rotation matrix, $R_{c,t}$ in Eq. (30), exploiting the knowledge of $\boldsymbol{v}_w$ and $R_{t,w}$, thus $\boldsymbol{v}_t$ (the LOS in terminator frame), by setting:

$$R_{c,t} = V_{\mathcal{T}} S V_T^T, \tag{33}$$

where V_T and $V_{\mathcal{T}}$ are the eigenvector matrices of $(T^* - \rho^2 \boldsymbol{v}_t \boldsymbol{v}_t^T)$ and $\mathcal{T}^*$, respectively. By definition, $\mathbf{n}_c$ is the third column of $R_{c,t}$. As with Eq. (21), Eq. (33) leaves sign ambiguities. After retaining the signs combinations leading to proper orthogonal matrices only, the correct S to be chosen is the one such that the equality:

$$\boldsymbol{v}_c = R_{c,t} \boldsymbol{v}_t, \tag{34}$$

is approximated with the closest matching.

Despite the two methods are theoretically equivalent, it was found from testing with images that estimating $\mathbf{n}_c$ from $R_{c,t}$ leads to better results. The reason is ascribed to the fact that the two ellipses, limb and terminator, are fitted independently, so that there is no guarantee that they share a common LOS $\boldsymbol{v}_c$. Plugging $\boldsymbol{v}_c$ as computed from the limb ellipse into Eq.(32) will thus introduce errors.

C. Attitude estimation from limb and terminator ellipse

Once two independent unit-vector observations are available, the attitude matrix can be computed from one of the many methods available in the literature, starting from e.g. a simple TRIAD algorithm, or any solution algorithm to Wahba problem (see e.g. [20]).

III. Numerical simulations

As a first step towards the validation of the revisited planet-Sun attitude determination method, we tested the algorithm against a Matlab®-based simulation environment by generating synthetic images of an illuminated object using the built-in image generation tool. This tool allows to create synthetic images of ellipsoids and polyhedral as imaged by pinhole cameras, with settable camera field of view and pose, illumination conditions, and surface properties.

We consider as example of triaxial ellipsoids the Saturnian moons Dione and Enceladus, which was repeatedly imaged by Cassini spacecraft during its long-lasting mission. To check the consistency of the algorithm under ideal conditions and to assess its potential maximum accuracy across a wide range of viewpoints and illumination conditions, we set up a Monte Carlo-like simulation. To this end, we first generated a set of synthetic images of Dione and Enceladus best-fit ellipsoids, as if they were captured by a camera having FoV equal to 30 deg.

The following angles variations were assumed:

- latitude of observation, between 0° and 90° with 30° step;

- longitude of observation, between 0° and 90° with 30° step;

- solar latitude, between -90° and +90° with 30° step;

- solar longitude, between -150° and +180° with 30° step;

All the possible combinations of the above angles for which the phase angle is not exceeding 150° have been explored[5], leading to a total of 2×452 images for the two Saturnian satellites. For each generated image, the attitude of the camera is prescribed as a sequence of two rotations: first the yaw angle is selected from a pseudo-random uniform distribution in the interval $[0 \ 2\pi]$. Then random off-nadir angles were prescribed with a normal distribution having zero mean and standard deviation equal to 3% of the camera FoV. The dimensionless range from the target was set equal to 5, leading to the ellipsoid occupying about 70% of the camera FOV.

---

[5] When phase angle exceeds 150°, the visible portion of the body is so thin that the limb arc is too short for a reliable ellipse fitting.

Afterwards, we repeated the above Monte Carlo-like simulations, this time generating images using a polyhedral shape model of Dione[6] [21]. This second step is aimed at addressing the performance degradation to be expected due to a target surface departing significantly from the one of an ellipsoid.

For both the ellipsoid and polyhedral images, illumination was simulated assuming an infinitely far away light source, ambient light was set to zero and the target surface was modelled as diffusely reflective with standard Gouraud shading. Before being processed for limb and terminator detection, all generated images were corrupted adding blur, through a 2-D Gaussian smoothing kernel having size of 3 pixels, plus unbiased gaussian noise afterwards. The standard deviation of the smoothing kernel and of gaussian noise were set to match, respectively, the full width at half maximum (FWHM) of the point spread function and the pixel signal to noise ratio stated for Cassini spacecraft Imaging Science Subsystem Narrow Angle Camera (ISS-NAC) [22], see Section IV.

The limb pixels were identified using a Canny edge detector with manually tuned thresholds (step a). Since the planetary limb is usually by far the strongest edge found in the image, this approach provides adequate results. For the terminator detection, a different approach was used, to cope with the fainter edge, as follows.

The grayscale image is converted to binary (black and white), then the edge detection algorithm is applied. This way, the entire outline of the binary image, i.e. the union of limb plus terminator, is detected (step b). Let n_l to be the number of limb pixels, and $n_o > n_l$ the number of outline pixels, and compute the $n_o \times n_l$ pairwise distance matrix of the limb pixels from the outline ones. For each outline pixel, the minimum among the distances to each limb pixel is recorded (i.e. the minimum element of each row in the pairwise distance matrix, step c). Finally, the outline pixel is labelled as belonging to the terminator if this minimum value is greater than a certain threshold.

The rationale for this criterion is that, if an outline pixel belongs to the limb of the *binary* image, it is then expected that there exists at least one limb pixel from the *grayscale* image very close to it (or, ideally, superimposed). The distance threshold can be related to the apparent size of the target within the image. In our tests, a heuristic threshold in the range 2-5% of the limb ellipse semi-major axis was found to be adequate. A step-by-step representation of the image processing algorithm described above is depicted in Fig. 4.

Once the limb and terminator pixel sets are created, they are fitted to ellipses using the method described in [23]. Finally, the algorithm presented in Section II is applied to each image to compute the LOS and illumination directions.

---

[6] The same test could not be made for Enceladus as we are not aware of a published polyhedral model.

Results are provided through the error angles α and β, defined as the angles between the true and the estimated directions. No algorithm is run to extract a triaxial attitude parametrization from the two observed directions, which would otherwise make the error evaluation process dependent on the specific method chosen.

Before discussing the error trends, it is worth to inspect the impact of the finite distance on the computation of the LOS direction, which has been qualitatively addressed in Section II.A for a sphere. To this end, Fig. 5 displays the distance in pixels between the projection of the ellipsoid center on the image plane and the center of the projected ellipse across the Monte Carlo test samples. The magnitude of such shift reaches values up to ≈6 pixels, an amount which would introduce a significant bias in the LOS when incorrectly adopting the imaged ellipse center as the LOS measure.
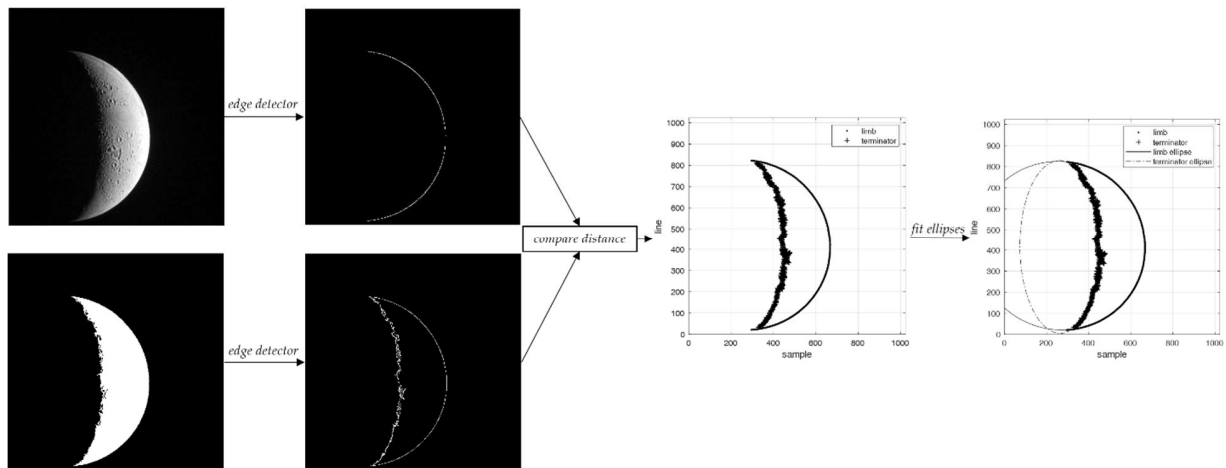

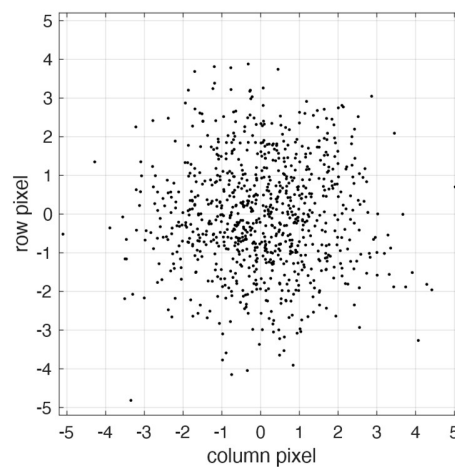**Fig. 4 Schematic overview of the image processing steps.**

Fig. 5 Pixel difference between the imaged ellipse center and the projected ellipsoid center across Monte Carlo simulations.

Table 1 Error statistics for the LOS and illumination directions errors from images of Dione and Enceladus best-fit ellipsoids.

	α [° (px)]			β [°]		
rms	68%	95%	*rms*	68%	95%	
0.008 (0.28)	0.007 (0.23)	0.018 (0.61)	0.15	0.15	0.31	

Inspection of Table 1 suggests that the proposed method can effectively estimate the LOS direction under varying illumination conditions, keeping the error smaller than one pixel in most cases. On the other hand, β error angle lies mostly in the range 0.1-0.2 degree, indicating that, as for other kinds of optical based attitude sensors, the planet-Sun attitude determination is more accurate in computing the LOS direction than the rotation about it.

Table 2 Error statistics for the LOS and illumination directions errors from images of Dione polyhedral shape model.

	α [° (px)]			β [°]		
rms	68%	95%	*rms*	68%	95%	
0.066 (2.25)	0.048 (1.65)	0.156 (5.32)	1.01	0.97	2.03	

When switching to the polyhedral shape model, see Table 2, the estimation accuracy drops significantly, as could have been expected. Both error angles increase by almost an order of magnitude: the nadir direction is now determined with a root mean squared accuracy of $\approx$ 2 pixels, while the *rms* for illumination direction raises to $\approx$1°. This is deemed, nevertheless, a good result given that the close-up views of Dione polyhedral surface feature extremely irregular terminator curves, as it is apparent from Fig. 6.

It is finally worth noting that, by varying the phase angle, different limb arc widths are made available in the image, going as low as 90° for phase angles of 150°. In our simulations, we found that the accuracy degrades significantly when the arc length falls below about 90° for the ideal ellipsoid, and about 120° for the polyhedral shape model. A few instances occurred for the shortest polyhedron arc lengths, where the ellipse fitting was essentially unsuccessful:

these were labelled as outliers, thus not considered for the statistics in Table 2. The number of outliers amounted to 16 out of 452 images.
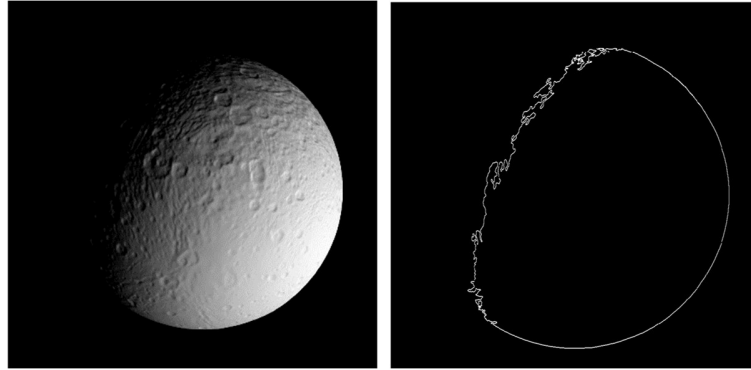

Fig. 6 Sample synthetic image of Dione shape model (left panel), and its outline (right panel), highlighting the irregular terminator curve.

IV. Validation against Cassini ISS-NAC images

To check the applicability of the method in real-word scenario such as a deep space mission, where the imaged target is only approximated by an ellipsoid, we tested the algorithm against a set of six images of Dione and Enceladus taken by Cassini ISS-NAC, and retrieved from the Planetary Data System[7], Fig. 7. The NAC 1024×1024 field of view (FOV) is approximately 0.53 deg wide (IFOV = 1.245 arcsec/px), with focal length 2003.4 mm; the experimental FWHM of the point spread function is 1.3 pixel, while the typical pixel SNR is 260 [22].

The satellites' semi-axes lengths, orientation with respect to the Sun direction, and relative position to Cassini have been retrieved from publicly available SPICE kernels [24]. The ground truth NAC attitude is computed from the stars found in each image. To this end, the database of stellar-based reconstructed attitude developed by Tajeddine et al. has been employed [25,26], which is greatly acknowledged. Relevant ground truth data for each image are collected in Table 3. Error angles α and β obtained after processing the images for limb and terminator detection and running the quadric-conic attitude algorithm, are collected in Table 4.

Results compare well with those obtained during the numerical validation phase, leading to $\alpha < 1.5$ pixels and $\beta < 1.2°$.

---

[7] https://pds.nasa.gov/.

Table 3. Cassini images used for test showing the following: image name, date and time of the image (UTC), target name, range, unit vector to target in camera frame, unit vector from target to the Sun in camera frame.

#	Target	image label	time	range [km]	$\boldsymbol{v}_c$	$\boldsymbol{s}_c$
1	Enceladus	N1569849851_1	2007-273 12:48:59.395	1.076406×10^8	[0.000018 -0.000258 0.999999]	[0.255752 -0.933246 -0.252274]
2	Enceladus	N1584034757_2	2008-072 17:02:25.623	1.051542×10^8	[0.001487 0.000533 0.999998]	[-0.902485 -0.000346 0.430719]
3	Enceladus	N1484519663_1	2005-015 22:08:16.377	3.6455124×10^8	[-0.000081 -0.000009 0.999999]	[0.866464 -0.415808 -0.276304]
4	Dione	N1569853047_1	2007-273 13:42:06.512	1.9829637×10^8	[0.000112 -0.000172 0.999999]	[0.792647 -0.582190 -0.181009]
5	Dione	N1584873547_1	2008-082 10:02:09.813	6.6638044×10^8	[-0.000389 -0.000383 0.999999]	[0.066704 -0.985256 0.157546]
6	Dione	N1489254498_1	2005-070 17:21:40.580	1.1548502×10^9	[-0.000222 -0.000115 0.999999]	[-0.877625 -0.380385 0.291686]
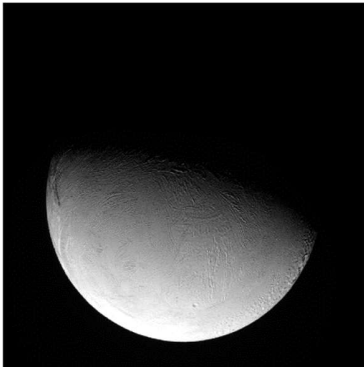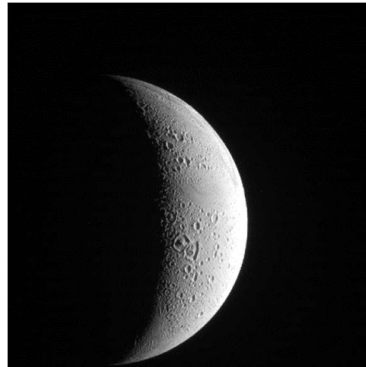
N1569849851_1   N1584034757_2   N1484519663_1

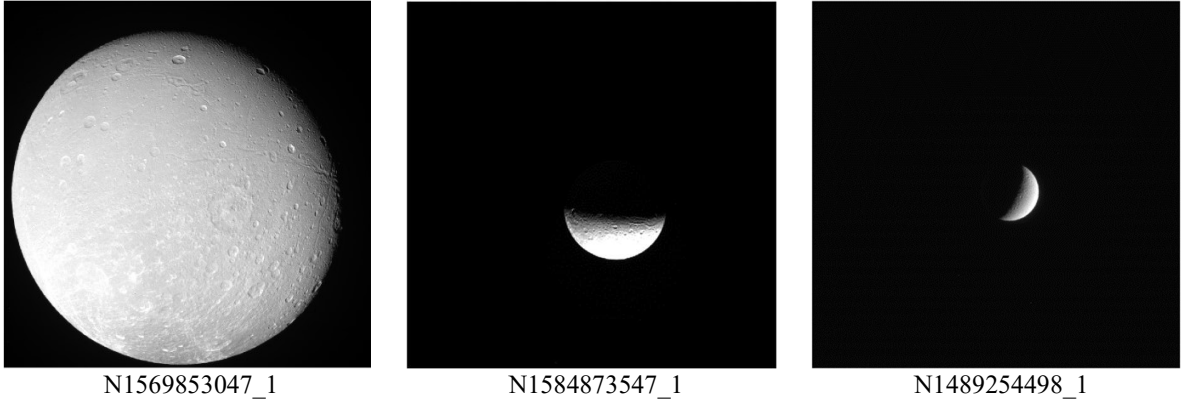| N1569853047_1 | N1584873547_1 | N1489254498_1 |

Fig. 7 Cassini ISS-NAC images used for checking the algorithm in a representative deep-space mission scenario: Enceladus (top panel), Dione (bottom panel).

Table 4. Errors for the LOS and illumination directions errors after processing of Cassini images.

#	Target	image label	α [°]	[px]	β [°]
1	Enceladus	N1569849851_1	5.622×10^{-4}	1.62	0.318
2	Enceladus	N1584034757_2	0.742×10^{-4}	0.22	0.415
3	Enceladus	N1484519663_1	3.462×10^{-4}	1.00	0.036
4	Dione	N1569853047_1	4.933×10^{-4}	1.44	0.636
5	Dione	N1584873547_1	3.250×10^{-4}	0.95	0.871
6	Dione	N1489254498_1	0.974×10^{-4}	0.28	1.10

V. Conclusions

A framework for the attitude determination from an illuminated ellipsoid was presented here to revisit the so-called planet-Sun attitude sensor concept, leading to a generalized quadric-conic sensor. The measurement process makes use of images of illuminated celestial bodies to compute the line-of-sight and Sun directions. These can then be combined using any algorithm for attitude determination from vector observations to compute the triaxial orientation of the imaging camera. The main assumption required to run the algorithms is that the target surface can be well approximated by the one of an ellipsoid whose orientation is known with respect to the illumination direction.

The attitude determination algorithm is first checked against synthetically generated images of triaxial ellipsoids resembling Saturn's moons Dione and Enceladus. Sensitivity of the algorithm accuracy under varying vantage points is then assessed through numerical simulations. Obtained results lead to *rms* error for the estimated LOS ranging of a fraction of a pixel. Applying the algorithm to an irregular surface, represented by a polyhedron, the LOS *rms* error increases to ≈ 2 pixels. Similarly, the *rms* error for the illumination direction spans from about $0.15°$ (ellipsoid) to $\approx 1°$ (polyhedron), suggesting that the accuracy for this angle is strongly affected by the irregular terminator shape generated by the craters-like features populating the surface. These results are in line with the ones reported for the moon tracking algorithm developed in [4] which, however, can be applied only to celestial bodies of spherical shape.

As a by-product, an analytical evaluation of the error committed in assuming the LOS coincident with the center of the imaged ellipse is also performed, showing that its magnitude is related to the range-to-planet size ratio, thus becoming increasingly significant for wide angle cameras.

The capability of the sensor concept to handle real-life scenarios is then assessed using some images of Dione and Enceladus gathered by Cassini Spacecraft and retrieved from NASA Planetary Data System. This test revealed an accuracy which is consistent with the predictions from the numerical validation, thus supporting the practical applicability of the quadric-conic attitude determination algorithm.

Our future efforts will be mainly devoted to a more extensive numerical testing, encompassing different celestial bodies.

Appendix

Consider an ellipsoid of revolution having known ellipticity $e = \sqrt{1 - c^2/a^2}$. In such a case, the first term of the right-hand side of Eq. (7) can be made explicit as:

$$R\breve{Q}_3^* R^T = R\text{diag}(k^2[1 \quad 1 \quad 1 - e^2])R^T = k^2 \begin{bmatrix} 1 - e^2 r_{13}^2 & -e^2 r_{13} r_{23} & -e^2 r_{13} r_{33} \\ -e^2 r_{13} r_{23} & 1 - e^2 r_{13}^2 & -e^2 r_{23} r_{33} \\ -e^2 r_{13} r_{33} & -e^2 r_{23} r_{33} & 1 - e^2 r_{33}^2 \end{bmatrix}, \tag{35}$$

where r_{ij} denotes the elements of R. As a result, the adjugate of $\mathcal{C}$ matrix reads:

$$\mathcal{C}^* \sim \begin{bmatrix} k^2(1 - e^2 r_{13}^2) - v_1^2 & -(e^2 k^2 r_{13} r_{23} + v_1 v_2) & -(e^2 k^2 r_{13} r_{33} + v_1 v_3) \\ -(e^2 k^2 r_{13} r_{23} + v_1 v_2) & k^2(1 - e^2 r_{23}^2) - v_2^2 & -(e^2 k^2 r_{23} r_{33} + v_2 v_3) \\ -(e^2 k^2 r_{13} r_{33} + v_1 v_3) & -(e^2 k^2 r_{23} r_{33} + v_2 v_3) & k^2(1 - e^2 r_{33}^2) - v_3^2 \end{bmatrix}. \tag{36}$$

Or, in terms of dimensionless conic center coordinates:

$$\frac{\mathcal{C}^*_{(i,3)}}{\mathcal{C}^*_{(3,3)}} = \frac{\nu_i}{\nu_3} \cdot \frac{1 + \frac{r_{i3}r_{33}}{\nu_i\nu_3}e^2k^2}{1 - k^2/\nu_3^2(1 - e^2r_{33}^2)} \quad i = 1,2 \tag{37}$$

which is the counterpart of Eq. (10), derived in II.A for a sphere, relating the LOS components ν_i to the center of the imaged ellipse.

References

1. Wabha, G. "A Least Squares Estimate for Spacecraft Attitude," *SIAM Review*, Vol. VII, No. 3, pp. 409-409, 1965. https://doi.org/10.1137/1007077

2. Mortari, D. "Moon-Sun Attitude Sensor", *Journal of Spacecraft and Rockets* Vol. 34, No. 3, 1997, pp. 360-364. https://doi.org/10.2514/2.3217.

3. Park, K.-J., Mortari, D., "Planet or Moon image processing for spacecraft attitude estimation," *J. Electron. Imag.*, Vol. 17, No 2, 023020, 2008. https://doi.org/10.1117/1.2938999.

4. Enright, J. "Moon-Tracking Modes for Star Trackers", *Journal of Guidance, Control, and Dynamics*, Vol. 33, No. 1, pp. 11-185, 2010.

5. Sekiguchi, T., Yamamoto, T., Iwamaru, Y. "3-Axes Attitude Estimation Experiments Using CCD Earth Sensor", *IFAC Proceedings Volumes*, Vol. 37, No. 6, pp. 741-746, 2004. https://doi.org/10.1016/S1474-6670(17)32265-6.

6. Modenini, D., "Attitude solution from Ellipsoid Observations: a modified Orthogonal Procrustes Problem", *Journal of Guidance, Control, and Dynamics*, Vol. 41 No. 10, pp. 2320-2325. https://doi.org/10.2514/1.G003610.

7. Modenini, D.; Locarini, A.; Zannoni, M. Attitude Sensor from Ellipsoid Observations: A Numerical and Experimental Validation. *Sensors* **2020**, *20*, 433. https://doi.org/10.3390/s20020433.

8. Hartley, R., and Zisserman, A., "Action of a projective camera on quadrics", *Multiple View Geometry in Computer Vision*, 2nd ed., Cambridge University Press, New York, 2004, pp. 201-202. https://doi.org/10.1017/CBO9780511811685.

9. Lightsey, G.E.; Christian, J.A. "Onboard image-processing algorithm for a spacecraft optical navigation sensor system", *Journal of Spacecraft and Rockets*, vol. 49, no. 2, pp. 952-958, 2012, pp. 337–352. http://dx.doi.org/10.2514/1.A32065

10. Christian, J.A., "Optical Navigation Using Planet's Centroid and Apparent Diameter in Image", *Journal of Guidance, Control, and Dynamics*, Vol. 38, No. 2 (2015), pp. 192-204. https://doi.org/10.2514/1.G000872

11. Christian, J.A., "Accurate Planetary Limb Localization for Image-Based Spacecraft Navigation", *Journal of Spacecraft and Rockets*, Vol. 54, No. 3, 2017, pp.708-730. doi:10.2514/1.A33692.

12. Mortari, D., de Dilectis, D., and Zanetti, R., "Position Estimation Using the Image Derivative", *Aerospace*, Vol. 2, No. 3, 2015, pp. 435-460. doi:10.3390/aerospace2030435.

13. Mortari, D., D'Souza, C.N., and Zanetti, R., "Image Processing of Illuminated Ellipsoid", *Journal of Spacecraft and Rockets*, Vol. 53, No. 3, 2016, pp. 448-456. https://doi.org/10.2514/1.A33342.

14. Modenini, D. "Five-Degree-of-Freedom Pose Estimation from an Imaged Ellipsoid of Revolution", *Journal of Spacecraft and Rockets*, vol. 56, no. 3, pp. 952-958, 2019. https://doi.org/10.2514/1.A34340.

15. J. A. Christian, "A Tutorial on Horizon-Based Optical Navigation and Attitude Determination With Space Imaging Systems," in *IEEE Access*, vol. 9, pp. 19819-19853, 2021, doi: 10.1109/ACCESS.2021.3051914.

16. Klein, P.P. "On the Ellipsoid and Plane Intersection Equation", *Applied Mathematics*, **3**, 1634-1640 (2012). https://doi.org/10.4236/am.2012.311226.

17. J. Wu, Y. Sun, M. Wang, and M. Liu, "Hand-eye Calibration: 4D Procrustes Analysis Approach," *IEEE Trans. Instrum. Meas.*, 2019. Doi 10.1109/TIM.2019.2930710.

18. Hansen, C.J., Caplinger, M.A., Ingersoll, A. *et al.* Junocam: Juno's Outreach Camera. *Space Sci Rev* **213,** 475–506 (2017). https://doi.org/10.1007/s11214-014-0079-x

19. Park, Ryan; Riedel, Ed. Advanced pointing imaging camera (APIC) concept. European Planetary Science Congress 2018, 16-21 September 2018 at TU Berlin, Berlin, Germany.

20. Markley, F.L. Equivalence of Two Solutions of Wahba's Problem. *J of Astronaut Sci* **60,** 303–312 (2013). https://doi.org/10.1007/s40295-015-0049-x

21. Gaskell, R.W., Gaskell Dione Shape Model V1.0. CO-SA-ISSNA/ISSWA-5-DIONESHAPE-V1.0. NASA Planetary Data System, 2013.

22. Porco, C.C., West, R.A., Squyres, S. et al. Cassini Imaging Science: Instrument Characteristics And Anticipated Scientific Investigations At Saturn. Space Sci Rev 115, 363–497 (2004). https://doi.org/10.1007/s11214-004-1456-7.

23. Szpak, Z. L., Chojnacki, W., van den Hengel, A., "Guaranteed ellipse fitting with a confidence region and an uncertainty, measure for centre, axes, and orientation," *Journal of Mathematical Imaging and Vision*, Vol. 52, No. 2, 2015, pp 173–199. http://dx.doi.org/10.1007/s10851-014-0536-x.

24. Acton, C., Bachman, N. Semenov, B. Wright, E. A look toward the future in the handling of space science mission geometry; Planetary and Space Science (2017); https://doi.org/10.1016/j.pss.2017.02.013

25. Tajeddine, R., Cooper, N. J., Lainey, V., Charnoz, S., & Murray, C. D. (2013). Astrometric reduction of Cassini ISS images of the Saturnian satellites Mimas and Enceladus. Astronomy & Astrophysics, 551, A129.

26. Tajeddine, R., Lainey, V., Cooper, N.J., et al. Cassini ISS astrometry of the Saturnian satellites: Tethys, Dione, Rhea, Iapetus, and Phoebe 2004-2012. Astronomy & Astrophysics., 575 (2015), p. A73.